Robotics and Computer–Integrated Manufacturing 49 (2018) 301–308

Contents lists available at ScienceDirect

Robotics and Computer–Integrated Manufacturing

journal homepage: www.elsevier.com/locate/rcim

# Calibration and decoupling of multi-axis robotic Force/Moment sensors

Qiaokang Liang[a,b,*], Wanneng Wu[a], Gianmarc Coppola[c], Dan Zhang[d], Wei Sun[a,b], Yunjian Ge[e], Yaonan Wang[a,b]

[a] College of Electrical and Information Engineering, Hunan University, Changsha, Hunan 410082, China
[b] National Engineering Laboratory for Robot Vision Perception and Control, Hunan University, Changsha, Hunan 410082, China
[c] Faculty of Engineering and Applied Science, University of Ontario Institute of Technology, Oshawa, Ontario L1H 7K4, Canada
[d] Department of Mechanical Engineering, York University, Toronto, ON M3J 1P3, Canada
[e] Institute of Intelligent Machines, Chinese Academy of Science, Hefei, Anhui 230031, China

ARTICLE INFO

*Keywords:*
Robotic sensory system
Multi-axis Force/Moment sensors
Calibration and decoupling
Extreme Learning Machine

ABSTRACT

Multi-axis robotic Force/Moment (F/M) sensors are capable of simultaneously detecting multiple components of force (Fx, Fy, and Fz), as well as the moments (Mx, My and Mz). This enables them to be frequently used in many robotic applications. Accurate, time-effective calibration and decoupling procedures are critical to the implementation of these sensors. This paper compares the effectiveness of decoupling methods based on Least-Squares (LS), BP Neural Network (BPNN), and Extreme Learning Machine (ELM) methods for improving the performance of multi-axis robotic F/M sensors. In order to demonstrate the effectiveness of the decoupling methods, a calibration and decoupling experiment was performed on a five-axis robotic F/M sensor. The experiments demonstrate that the ELM based decoupling method is superior to LS and BPNN based methods. The presented theoretical and experimental demonstrations provide a comprehensive description of the calibration and decoupling procedures of multi-axis robotic F/M sensors. This work reveals that the ELM method is an appropriate and high performing decoupling procedure for multi-axis robotic F/M sensors.



## 1. Introduction

Multi-axis robotic Force/Moment (F/M) sensing is an important branch of robotic sensing intended to measure the external forces and moments on robotic manipulators. Multi-axis sensing has been widely considered in both industry and academic research and also plays an increasing role in the fields of robotics, haptics, virtual reality, etc. in order to acquire relevant information from physical interactions [1,2]. Recently, researchers have investigated and developed many F/M sensing systems with adequate performance via both direct and indirect approaches [3,4]. A six-axis F/M sensor can measure the tangential force terms along x-, y-, and normal force term along z-axis (Fx, Fy, and Fz) as well as the moment terms about x-, y-, and z-axis (Mx, My, and Mz) simultaneously [5]. Multi-axis F/M sensors refer to sensors that can detect less than the six terms, to which the most commonly used F/M sensors are three-, or six-axis [6–8].

The trend towards flexibility in manipulation and effective control progressively requires high performance multi-axis F/M sensors in robotics and automation. For this purpose, continuous improvement approaches have been attempted. In this process, much of the research has revealed interesting scientific questions and technological challenges in developing high-precision and robust F/M sensing systems. Several researchers have designed a wide variety of multi-axis F/M sensors with novel structures in order to improve the sensing accuracy. For example, Meng et al. presented a novel six-axis accelerometer based on a structure of dual annular membranes [9].

Precise calibration and decoupling of multi-axis F/M sensor is critical and can be challenging. More specifically, the calibration process of multi-axis F/M sensors refers to the relationship between the sensors output voltages and the applied load. This relationship should be accurate and reliable according to the applied standard and maintain a certain accuracy of measurement. Also, the majority of the existing multi-axis F/M sensors have inherent highly coupled interference errors among their components (especially between component $F_x$ and component $M_y$, component $F_y$ and component $M_x$ respectively), which are influenced by the sensing principle, manufacturing process, EE structure and detection mode [7,10,11]. The coupling effect produces a significant decrease in accuracy of the sensor and requires complicated decoupling algorithms for compensation [12,13]. Therefore, particular emphasis has been given to the decoupling algorithms of multi-axis F/M sensors [15].

Wu and Cai [16] constructed a unique six-axis F/M sensor to measure the interactive force between surgical tools and soft tissue. This can ide-

* Corresponding author.
*E-mail address:* qiaokang@mail.ustc.edu.cn (Q. Liang).

http://dx.doi.org/10.1016/j.rcim.2017.08.008
Received 28 May 2016; Received in revised form 28 July 2017; Accepted 10 August 2017
Available online 14 August 2017
0736-5845/

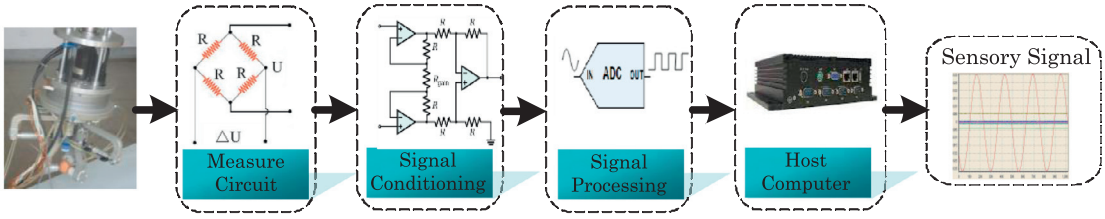


**Fig. 1.** Schematic illustration of a multi-axis F/M sensor.

ally be used for haptic information acquisition in virtual surgery. The authors proposed a novel Elastic Element (EE) based on a decoupling mechanism with that has a sliding structure. The calculated expanded uncertainty and coupling error of the sensor are 0.1% F.S. and 0.89% F.S, respectively. Yuan et al. [8] constructed a six-axis F/M sensor based on a typical EE with double cross-beam structures for humanoid robot foot. This sensor is capable of over 1000 N of total vertical load, and after linear static decoupling, its repeatability error and interference error are less than 1.88% F.S. and 3.0% F.S., respectively. Dasgupta et al. [17] disclosed a design methodology for the Stewart platform sensor structure based on the optimal conditioning of the force transformation matrix. Unlike the traditional EEs that measure all the F/T components with a single monolithic structure, this kind of sensor employs limbs of the parallel mechanism to detect the F/M components. This uniquely makes it possible to provide de-coupling F/M information with high stiffness and high sensitivity. Recently, a nonlinear static decoupling algorithm based on a coupling error model and six separate Support Vector Regressions (SVRs) for 3-axis force sensors was proposed. In this study, the maximum interference error was claimed to be within 1.6% F.S. [18].

In this paper, we study the theoretical and experimental demonstrations of several proposed decoupling methods such as LS, BPNN, and ELM. Calibration and decoupling experiments with the proposed methods are carried out on a five-axis F/T sensor, and the results are compared and discussed.

## 2. Multi-axis F/M sensor system and its fundamental principle

Configurations adopted in multi-axis F/M sensors originate from various measurement principles such as resistive, capacitive, inductive, piezoelectric, magnetic and optical methods [19]. The most commonly used approaches out of these principles relies on resistive or piezoresistive measuring. The most well-known resistive transducers utilized on multi-axis F/M sensors are strain gauges. The measurement chain of the multi-axis F/M sensor system that uses the resistive method consists of several blocks, which can be observed in Fig. 1.

When bonded onto the EE of the sensor, the strain gauges will undergo changes of resistance that correspond to the deformation of the EE. This relationship is given by

$$\Delta R_i = G\varepsilon_i R_i \tag{1}$$

where $R_i$ is the original resistance of the $i$th strain gauge, G and $\varepsilon_i$ are the gauge factor and the strain, respectively. Provided that the EE behaves within the elastic range of the material, the occurred strain, $\varepsilon_i$, and the applied load, $L$, are related by the following equation:

$$\varepsilon_i = f_i(L) \tag{2}$$

Full-bridge measure circuits are always used to detect the small resistive changes with high sensitivity and inherent linearity. The output voltage of the $j$th bridge can be expressed as

$$\Delta U_j = \frac{1}{4}U_e G(\varepsilon_{j1} - \varepsilon_{j2} + \varepsilon_{j3} - \varepsilon_{j4}) \tag{3}$$

where $U_e$ denotes the voltage excitation source, and $\varepsilon_{jk}$ represent the strain in the $k$th gauge of the $j$th full-bridge circuit.

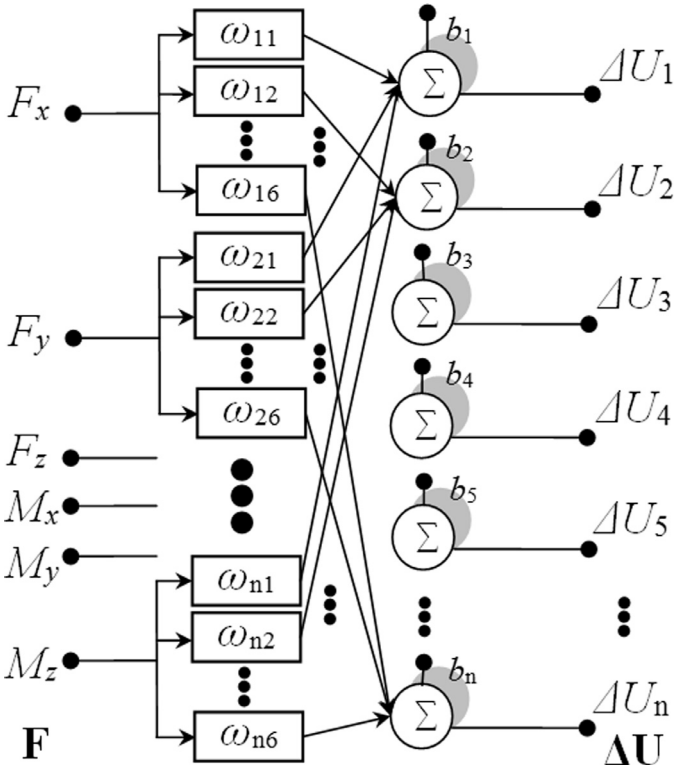


**Fig. 2.** Coupling model of multi-component F/M sensor.

Regarding multiple axis F/M sensors, several components will simultaneously generate output signals when a single F/M component is applied onto the sensor. This is mainly caused by the monolithic structure of the EE and the inherent manufacturing error. The coupling model of the multi-component F/M sensor is illustrated in Fig. 2.

Therefore, the output of the sensor composed of $n$ full-bridge circuits $\Delta\mathbf{U} \in \Re^n$ can be expressed as

$$\Delta\mathbf{U} = \mathbf{wF} + \mathbf{b} \tag{4}$$

where $\mathbf{w} \in \Re^{n\times m}$ and $\mathbf{b} \in \Re^n$ represent the coupling coefficient and bias matrices, respectively, and $\mathbf{F} \in \Re^m$ represents the applied load vector that contains three force components and three moment components applied to the center of the sensor. The output can also be expressed as

$$\Delta\mathbf{U} = \mathbf{TF} \tag{5}$$

where $\mathbf{T} \in \Re^{n\times m}$ is the transformation matrix, which depend on the structure and geometrical dimensions of the EE, the particular locations, and the configuration of the strain gauges bonded on the EE.

Signal conditioning of the F/M sensor includes amplification, isolation, thermal compensation, filtering, and range matching to qualify and enhance the sensor output $\triangle\mathbf{U}$ to be suitable for processing.

The main challenge in processing the signals from the F/M measurement is related to the methods used to extract useful information from

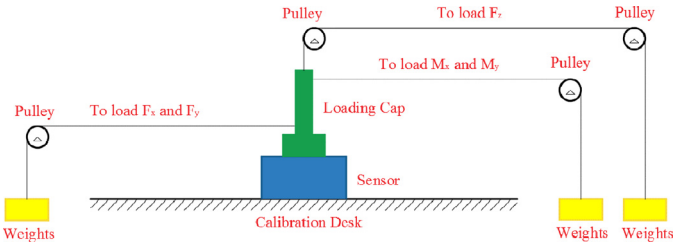


**Fig. 3.** Calibration setup and decoupling procedure of the multi-axis F/M sensor.

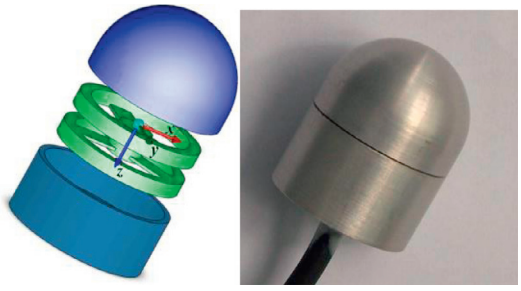


**Fig. 4.** Five-axis robotic F/M sensor: (a) Sketch of the sensor structure; (b) five-axis F/M sensor prototype.

the obtained sensor output signal. It is typically in the microvolt range which can provide a challenge. A microprocessor or a host computer is utilized to acquire and process the F/M information, as well as to present the measurement data in a manner that is useful for human interpretation. One of the most important tasks in processing the signals from the sensor is related to the determination of the relationship between the raw output signals and the actual applied load vector. This is also referred to as Calibration and Decoupling. The successful implementation of multi-axis F/M sensors in robotic systems depends primarily on the level of understanding associated with their calibration and decoupling methods.

## 3. Calibration and decoupling methods

Precise calibration and decoupling of multi-axis F/M sensor systems is critical and can be challenging. The most commonly utilized calibration procedure for the multi-axis F/M sensor begins by applying known reference forces or moment components individually to the sensor from the minimum to maximum measurement range with a constant increment. Meanwhile, the sensor output (volts) is monitored and recorded at each set point accordingly. After repeating the mentioned procedure five times in a cyclical pattern, the recorded data can be utilized to calibrate and decouple the sensor via the chosen method. The calibration setup and decoupling procedure of the sensor, as shown in Fig. 3, was performed as follows:

1. Firmly fix the sensor to the calibration platform with a loading cap bolted on its top.
2. Adjust the zero point of the output voltages of each component of the sensor.
3. Apply different weights on each component of the sensor within its measurement range, first gradually increasing to the positive full scale, and then decreasing to zero. Meanwhile, the output voltages of each component are recorded as samples.
4. The loading cycle is performed five times for each component.

A five-axis F/M sensor with a coupling error of 3% F.S. and a maximum relative error of 5% F.S. has been developed by our research team (as shown in the Fig. 4) [20].

The five-axis robotic F/M sensor used in this calibration experiment can measure the three contact forces along all three Cartesian coordinates (Fx, Fy, and Fz) and the according moments about two tangential axes (Mx and My). It behaves with good performance when measuring a single force or moment component. However, when the measurement is not limited to one force or moment there exists high coupling error among the F/M components. This is observed in Fig. 5. The coupling error makes it difficult to perform highly accurate multi-axis F/M measurements.

The following sections will focus on understanding various linear and nonlinear decoupling methods, as well as the corresponding experiments that were used to determine the optimal method. This knowledge strives to improve the performance of the multi-axis F/M sensor system.

### 3.1. Linear static calibration and decoupling method

Multi-axis F/M sensors convert the applied load **F** to an output vector $\triangle\mathbf{U}$. If the sensor is linear, the applied load can then be derived as follows:

$$\mathbf{F} = \mathbf{T}^{\#}\Delta\mathbf{U} + (\mathbf{I} - \mathbf{T}^{\#}\mathbf{T})\mathbf{z} \tag{6}$$

where $\mathbf{T}^{\#} \in \Re^{m\times n}$ is the generalized inversion of transformation matrix **T** and **z** is an arbitrary n × 1 vector. Usually the component number of the multi-axis F/M sensor, *m,* is less than or equal to 6 (such as 3-axis, 4-axis, and 6-axis F/M sensor), while the full-bridge circuits number, *n,* should be greater than or equal to *m*.

The Least-Squares (LS) technique, the most common method used for linear static decoupling of multi-axis F/M sensors, has been widely used for identification and calibration. This is done using a wide set of known F/M vectors (i.e., $\mathbf{F}_i$ carefully selected to adequately span the sensor measurement range) and the corresponding output vectors $\Delta\mathbf{U}_i$.

Assuming the calibration data ($\mathbf{F}_i$, $\Delta\mathbf{U}_i$) is available, and the output signals retrieved from the sensor can be expressed as follows:

$$\begin{bmatrix}\Delta\mathbf{U}_1^T\\ \Delta\mathbf{U}_2^T\\ \vdots\\ \Delta\mathbf{U}_p^T\end{bmatrix} = \begin{bmatrix}\mathbf{F}_1^T & 1\\ \mathbf{F}_2^T & 1\\ \vdots & \vdots\\ \mathbf{F}_p^T & 1\end{bmatrix}\begin{bmatrix}\mathbf{w}^T\\ \mathbf{b}^T\end{bmatrix} \tag{7}$$

Therefore, the coupling coefficient and bias matrices can be obtained as

$$\begin{bmatrix}\mathbf{w}^T\\ \mathbf{b}^T\end{bmatrix} = \left(\begin{bmatrix}\mathbf{F}_1 & \mathbf{F}_2 & \cdots & \mathbf{F}_p\\ 1 & 1 & \cdots & 1\end{bmatrix}\begin{bmatrix}\mathbf{F}_1^T & 1\\ \mathbf{F}_2^T & 1\\ \vdots & \vdots\\ \mathbf{F}_p^T & 1\end{bmatrix}\right)^{-1}\begin{bmatrix}\mathbf{F}_1 & \mathbf{F}_2 & \cdots & \mathbf{F}_p\\ 1 & 1 & \cdots & 1\end{bmatrix}\begin{bmatrix}\Delta\mathbf{U}_1^T\\ \Delta\mathbf{U}_2^T\\ \vdots\\ \Delta\mathbf{U}_p^T\end{bmatrix} \tag{8}$$

where *p* represents the total number of calibration data.

$$\begin{bmatrix}\mathbf{w}^T\\ \mathbf{b}^T\end{bmatrix} = \begin{pmatrix}\sum_{i=1}^{p}\mathbf{F}_i\mathbf{F}_i^T & \sum_{i=1}^{p}\mathbf{F}_i\\ \sum_{i=1}^{p}\mathbf{F}_i^T & p\end{pmatrix}^{-1}\begin{pmatrix}\sum_{i=1}^{p}\mathbf{F}_i\Delta\mathbf{U}_i^T\\ \sum_{i=1}^{p}\Delta\mathbf{U}_i^T\end{pmatrix} \tag{9}$$

the coupling coefficient and bias matrices can be written as

$$\mathbf{w}^T = \mathbf{A}\sum_{i=1}^{p}\mathbf{F}_i\Delta\mathbf{U}_i^T - \mathbf{A}\mathbf{B}\sum_{i=1}^{p}\Delta\mathbf{U}_i^T \tag{10}$$

$$\mathbf{b}^T = -\mathbf{B}^T\mathbf{A}\sum_{i=1}^{p}\mathbf{F}_i\Delta\mathbf{U}_i^T + \left(\mathbf{B}^T\mathbf{A}\mathbf{B} + 1/p\right)\sum_{i=1}^{p}\Delta\mathbf{U}_i^T \tag{11}$$

with

$$\mathbf{A} = \left(\sum_{i=1}^{p}\mathbf{F}_i\mathbf{F}_i^T - 1/p\sum_{i=1}^{p}\sum_{j=1}^{p}\mathbf{F}_i\mathbf{F}_j^T\right)^{-1} \tag{12}$$

$$\mathbf{B} = 1/p\sum_{i=1}^{p}\mathbf{F}_i \tag{13}$$

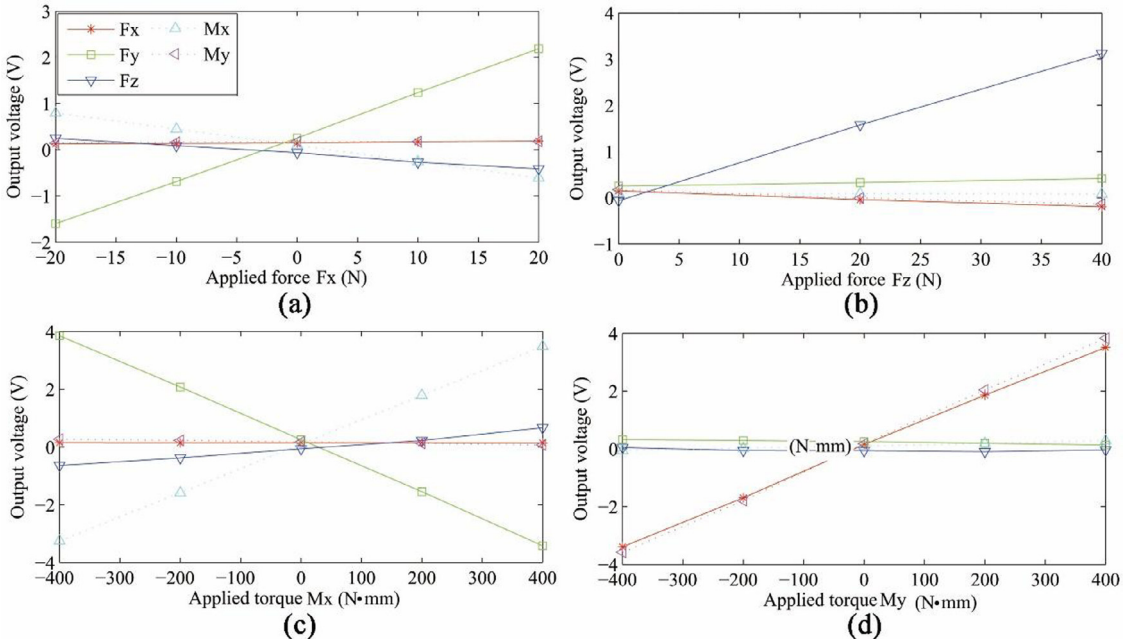


**Fig. 5.** The robotic five-axis F/M sensor outputs with coupling: (a) output of component Fx (similar with Fy); (b) output of component Fz; (c) output of component Mx; (d) output of component My.

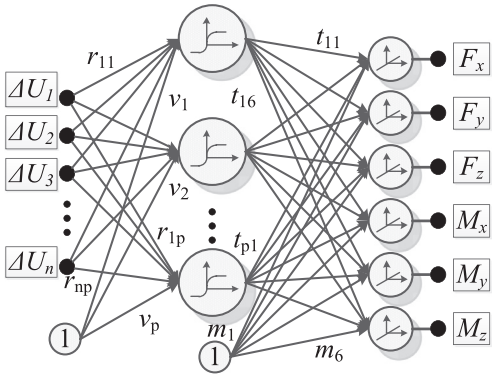


**Fig. 6.** Architecture of the BP NN for predicting multi-axis F/M.

The precision of the results obtained with this method depends on the accuracy and distribution of the obtained calibration data. It also illustrates that there needs to be a large amount of calibration data (with precise application of many known load vectors) in order to be useful for estimating coupling error. It can be challenging to achieve an optimal trade-off between the coupling error elimination and the execution time of data collection.

### 3.2. Decoupling method based on BP Neural Network (NN)

The F/M sensor output is susceptible to nonlinearity inherited from the EE device, interference as well as hysteretic behavior. As a consequence, a linear static calibration and decoupling method can be time-consuming and sometimes not possible.

Artificial Neural Networks, designed as a computational model, have been applied successfully in a wide range of applications due to their ability to accurately model systems in demanding real-time operation [21]. A BP NN with a single hidden layer of 13 fully connected units is used to predict the multi-axis F/M as illustrated in the Fig. 6.

The sigmoid function of the hidden nodes is represented by:

$$f(net) = \frac{2}{1 + e^{-2 \cdot net}} - 1 \tag{14}$$

The linear activation function $g$ is selected for the output nodes. The NN function with $p$ hidden nodes can be expressed as

$$\mathbf{L} = g(\mathbf{t}\, f(\mathbf{r}\Delta\mathbf{U} + \mathbf{v}) + \mathbf{m}) \tag{15}$$

where $\mathbf{L} = [\mathrm{Fx}, \mathrm{Fy}, \mathrm{Fz}, \mathrm{Mx}, \mathrm{My}, \mathrm{Mz}]^{\mathrm{T}}$, $\mathbf{r}$ and $\mathbf{t}$ represent weight matrices of the hidden layer and the output layer, respectively, $\mathbf{v}$ and $\mathbf{m}$ are bias matrices of the hidden layer and the output layer, respectively. The universal approximation capability of BP NN with sufficient hidden nodes enables its ability to approximate a nonlinear function. After the NN is sufficiently trained with the calibration data, it can be utilized to detect the applied F/M. The number of hidden layer nodes has a large impact on the prediction precision because too few or too many nodes will cause large prediction error that can be associated with the over-fit phenomena. The number of hidden layer nodes is initially set between 6 and 15 in this study. As shown in Fig. 7, the mean square error of the output dramatically decreases with an increase in the number of hidden layer nodes until it reaches 13, at which point the computation time arrives at its minimum.

### 3.3. Decoupling method based on Extreme Learning Machine algorithm (ELM)

ELM was proposed by Huang et al. [22] as a learning algorithm for a single hidden layer feed-forward neural network, as shown in Fig. 8. Unlike the traditional BP algorithm, the ELM randomly chooses the connection weights between the input layer and hidden layer, as well as the bias of hidden layer neurons. It has been widely implemented in pattern recognition, computer vision, data mining, signal processing, and control systems due to its extremely fast learning speed and outstanding overall performance.

Generally, the decoupling method of multi-axis F/M sensors can be deduced in the following manner. Suppose that there are $N$ calibration samples $\{\boldsymbol{u}_i, \boldsymbol{f}_i\}$, where $\boldsymbol{u}_i = [u_{i1}, u_{i2}, u_{i3}, u_{i4}, u_{i5}, u_{i6}]^{\mathrm{T}}$ is a multi-dimensional input (reaches the maximum at 6 when the F/M sensor has 6 axes) for every sample $i$ and $\boldsymbol{f}_i = [f_{i1}, f_{i2}, f_{i3}, f_{i4}, f_{i5}, f_{i6}]^{\mathrm{T}}$ is a multi-dimensional output for every sample $i$. The input and output represent the F/M sensor full-bridge output voltages and applied load vector respectively. The number of the hidden layer neurons, $L$, is derived from

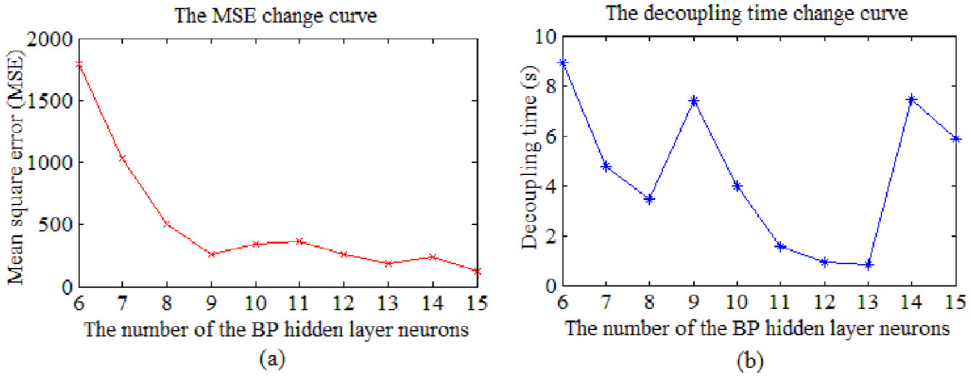


**Fig. 7.** Mean square error (a) and computation time (b) of the neural network training versus number of the neurons of hidden layer.

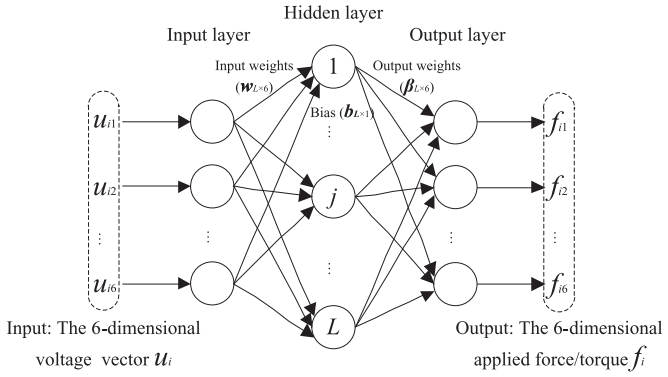


**Fig. 8.** The network structure diagram of ELM decoupling.

experiments. The output of a network with $L$ hidden nodes and an activation function $g(x)$ can be described as

$$\boldsymbol{t}_i = \begin{bmatrix} t_{i1} \\ t_{i2} \\ \vdots \\ t_{i6} \end{bmatrix}_{6\times1} = \begin{bmatrix} \sum_{j=1}^{L} \beta_{j1} g(\boldsymbol{w}_j \cdot \boldsymbol{u}_i + b_j) \\ \sum_{j=1}^{L} \beta_{j2} g(\boldsymbol{w}_j \cdot \boldsymbol{u}_i + b_j) \\ \vdots \\ \sum_{j=1}^{L} \beta_{j6} g(\boldsymbol{w}_j \cdot \boldsymbol{u}_i + b_j) \end{bmatrix}_{6\times1} = \sum_{j=1}^{L} \boldsymbol{\beta}_j g(\boldsymbol{w}_j \cdot \boldsymbol{u}_i + b_j), i = 1, ..., N \tag{16}$$

where $\boldsymbol{w}_j = [w_{1j}, w_{2j}, ..., w_{6j}]^{\mathrm{T}}$, $b_j$ and $\boldsymbol{\beta}_j = [\beta_{j1}, \beta_{j2}, ..., \beta_{j6}]^T$ represent the input weights, bias and output weights of the $j$th hidden layer neurons, respectively. The ELM reliably approximates N samples with minimum error following the relationship

$$\sum_{j=1}^{L} \boldsymbol{\beta}_j g(\boldsymbol{w}_j \cdot \boldsymbol{u}_i + b_j) = \boldsymbol{f}_i, i = 1, ..., N \tag{17}$$

The formula (17) can be rewritten as the following matrix form

$$\mathrm{H}\boldsymbol{\beta} = \boldsymbol{F} \tag{18}$$

where the matrix H is referred to be the hidden layer output matrix of the network

$$\mathrm{H}(\boldsymbol{w}_1, \boldsymbol{w}_2, ..., \boldsymbol{w}_L, b_1, b_2, ..., b_L, \boldsymbol{u}_1, \boldsymbol{u}_2, ..., \boldsymbol{u}_N) = \begin{bmatrix} g(\boldsymbol{w}_1 \cdot \boldsymbol{u}_1 + b_1) & g(\boldsymbol{w}_2 \cdot \boldsymbol{u}_1 + b_2) & \cdots & g(\boldsymbol{w}_L \cdot \boldsymbol{u}_1 + b_L) \\ g(\boldsymbol{w}_1 \cdot \boldsymbol{u}_2 + b_1) & g(\boldsymbol{w}_2 \cdot \boldsymbol{u}_2 + b_2) & \cdots & g(\boldsymbol{w}_L \cdot \boldsymbol{u}_2 + b_L) \\ \vdots & \vdots & \ddots & \vdots \\ g(\boldsymbol{w}_1 \cdot \boldsymbol{u}_N + b_1) & g(\boldsymbol{w}_2 \cdot \boldsymbol{u}_N + b_2) & \cdots & g(\boldsymbol{w}_L \cdot \boldsymbol{u}_N + b_L) \end{bmatrix}_{N\times L} \tag{19}$$

$$\boldsymbol{\beta} = \begin{bmatrix} \beta_1^T \\ \beta_2^T \\ \vdots \\ \beta_L^T \end{bmatrix}_{L\times6}, \boldsymbol{F} = \begin{bmatrix} f_1^T \\ f_2^T \\ \vdots \\ f_N^T \end{bmatrix}_{N\times6} \tag{20}$$

Therefore, the output weights $\boldsymbol{\beta}_{L\times6}$ can be found analytically by minimizing the error function $\zeta$ with randomly allocated input weights $\boldsymbol{w}_{L\times6} = [\boldsymbol{w}_1, \boldsymbol{w}_2, \cdots \boldsymbol{w}_L]^{\mathrm{T}}$ and hidden bias values $\boldsymbol{b}_{L\times1} = [b_1, b_2, \cdots, b_L]^{\mathrm{T}}$ for a given number of hidden neurons.

$$\zeta = \sum_{i=0}^{N} \|\boldsymbol{t}_i - \boldsymbol{f}_i\| \tag{21}$$

Moreover, the output weights of hidden layer neurons ($\boldsymbol{\beta}_{L\times6}$) can be acquired by solving the least-square norm solution,

$$\left\|\mathrm{H}\hat{\boldsymbol{\beta}} - \boldsymbol{F}\right\| = \min_{\boldsymbol{\beta}} \|\mathrm{H}\boldsymbol{\beta} - \boldsymbol{F}\| \tag{22}$$

Finally, the least-square norm solution of the output weights reduces to

$$\hat{\beta} = \mathrm{H}^{+}\boldsymbol{F} \tag{23}$$

where $\mathrm{H}^{+}$represents Moore–Penrose generalized inverse matrix of the matrix H.

According to the above analysis, the training procedure of the ELM decoupling method can be concluded as follows:

(1) Randomly allocate the input weights ($\boldsymbol{w}_{L\times6}$) and bias ($\boldsymbol{b}_{L\times1}$) for the hidden layer neurons.
(2) Calculate the hidden layer output matrix H.
(3) Calculate the output weights of the hidden layer neurons with $\hat{\beta} = \mathrm{H}^{+}\boldsymbol{F}$.

According to the theorem justified in Huang [22], if the number of hidden neurons are equal to the training sample number, the above network would approximate the training sample with zero error for any randomly chosen $\boldsymbol{w}_{L\times6}$ and $\boldsymbol{b}_{L\times1}$. However, when the sample number, $N$, is very large, the number of hidden layer neurons, $L$, is typically small in comparison to $N$ in order to reduce calculation effort. Initially, we chose to use 20–50 hidden neurons, and determined through experiments that the MSE of the predicted value and the computation time reach their optimal values when the number reaches 35, as shown in Fig. 9.

## 4. Results

For the experimental comparison of the proposed decoupling methods, a calibration and decoupling procedure of a robotic five-axis F/M sensor was performed. The data recorded in the calibration and decoupling experiment is normalized and then used as training data to test inputs and outputs. We selected 80% of the total set for training the BP

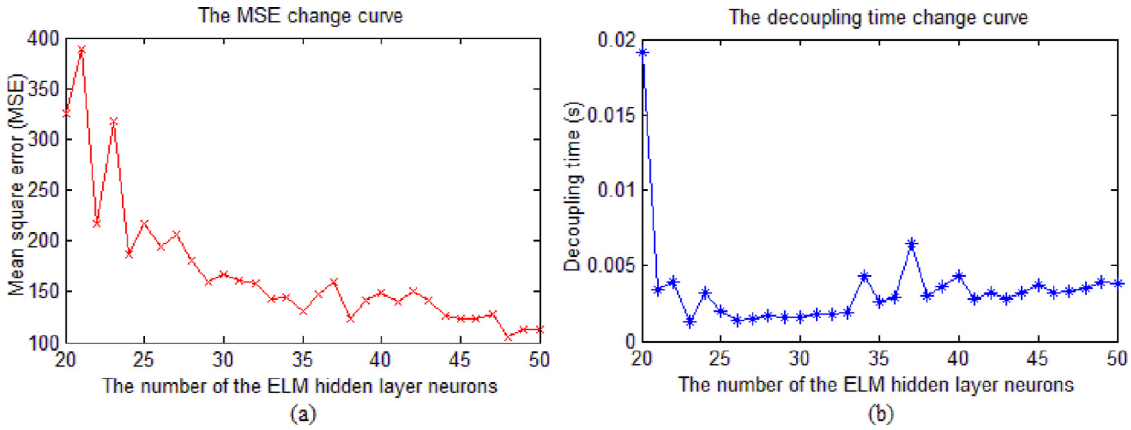


**Fig. 9.** The selection of the ELM network's hidden layer neurons number according: (a) the mean square error (MSE) of the predicted value with ELM; (b) the decoupling running time based on ELM algorithm.

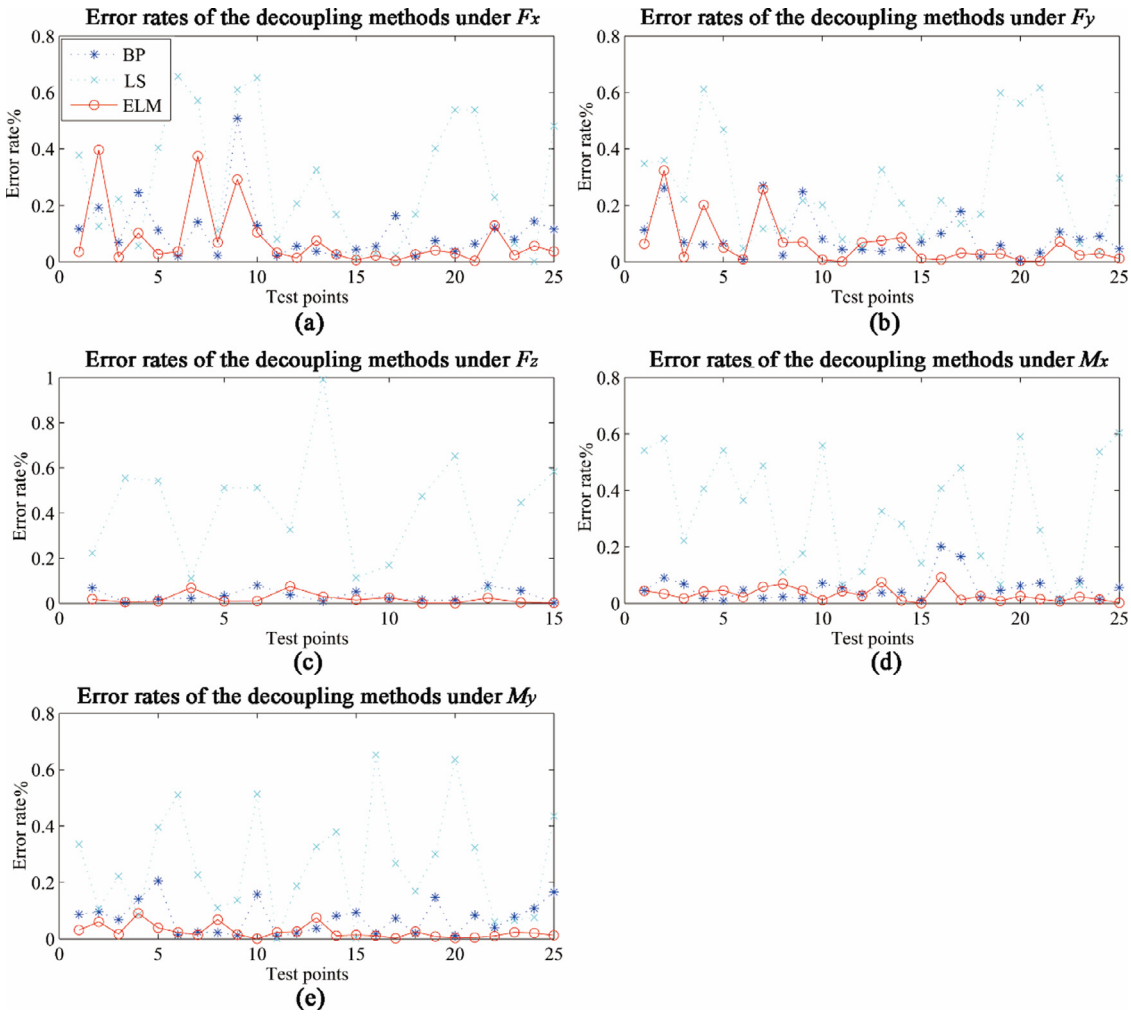


**Fig. 10.** Error rates of the decoupling methods under component Fx (a), Fy (b), Fz (c), Mx (d), and My (e).

NN and ELM, and utilized the remaining 20% of the set to test the decoupling methods. As illustrated in Fig. 10, the ELM and BPNN based decoupling methods are consistently superior to the LS based method, and the BPNN method is very comparable with, but not as accurate, to the ELM method.

The mean error rates of the three decoupling methods are summarized in Table 1. The maximum mean error rates of the LS, BPNN, and ELM are 9.39%, 0.16%, and 0.18%, respectively. Although the maximum mean error rate of the ELM is larger than that of BPNN method, the accuracy of the sensor with the ELM decoupling method is consistently better than the BPNN method. In general, the results show that there is a significant improvement in the accuracy of the multi-axis F/M sensor with the BPNN and ELM decoupling methods.

**Table 1**
Results of the decoupling methods.

| | | Mean error rates of the LS method results (%) | | | | |
|---|---|---|---|---|---|---|
| | | Fx | Fy | Fz | Mx | My |
| Component of the multi-axis F/M sensor | Fx | 0.406277 | 0.887277 | 1.208629 | 0.15437 | 0.1797419 |
| | Fy | 1.210813 | 1.518854 | 1.069594 | 0.164438 | 0.53743255 |
| | Fz | 1.916879 | 5.256272 | 9.393737 | 0.893552 | 2.72386586 |
| | Mx | 0.333648 | 0.844161 | 1.852485 | 0.188827 | 0.20264124 |
| | My | 1.319024 | 0.323774 | 1.597878 | 0.099907 | 0.70437202 |
| | | Mean error rates of the BPNN method results (%) | | | | |
| | | Fx | Fy | Fz | Mx | My |
| Component of the multi-axis F/M sensor | Fx | 0.147007 | 0.163862 | 0.036315 | 0.069732 | 0.1041335 |
| | Fy | 0.113939 | 0.125753 | 0.048917 | 0.071794 | 0.07039425 |
| | Fz | 0.029747 | 0.04493 | 0.032613 | 0.016043 | 0.04558526 |
| | Mx | 0.046139 | 0.034907 | 0.035081 | 0.09889 | 0.04618616 |
| | My | 0.119422 | 0.046062 | 0.048731 | 0.053739 | 0.09551147 |
| | | Mean error rates of the ELM method results (%) | | | | |
| | | Fx | Fy | Fz | Mx | My |
| Component of the multi-axis F/M sensor | Fx | 0.115497 | 0.175094 | 0.030389 | 0.024535 | 0.04926632 |
| | Fy | 0.131123 | 0.082495 | 0.04847 | 0.019178 | 0.02742444 |
| | Fz | 0.00993 | 0.029112 | 0.039664 | 0.009201 | 0.0096173 |
| | Mx | 0.036472 | 0.041075 | 0.030918 | 0.032761 | 0.01212463 |
| | My | 0.047884 | 0.024466 | 0.029846 | 0.010353 | 0.01428644 |

**Table 2**
The comparison of the decoupling algorithms respectively based on LS, BP and ELM.

| Decoupling algorithms | Advantages | Disadvantages | Running speed | Generalization performance |
|---|---|---|---|---|
| LS | Easy to perform | (1) Depends on a set of data that covers most of the measurement range of the sensor.<br>(2) The relationship between the applied weights and output voltages is not completely linear. | Relatively fast | Bad |
| BPNN | Theoretically able to map an arbitrary nonlinear relationship | (1) Too many parameters including the network layer number, neurons number, initial weights and learning rate, all of which are hard to be determined.<br>(2) Easy to fall into a local minimum point.<br>(3) Generalization performance is largely dependent on the training samples.<br>(4) A long training time due to the continuous iteration process. | Very slow | Relatively good |
| ELM | Extremely fast learning speed and good generalization performance. | (1) It is difficult to determine the number of the hidden layer neurons, which greatly influence the ELM network.<br>(2) Too many hidden layer neurons will cause the over-fitting problem. | Extremely fast | Good |

## 5. Discussion and conclusions

This paper presents both theoretical and experimental results on the comparison of several decoupling methods for multi-axis F/M sensors. The performance comparison of the three decoupling algorithms is illustrated in Table 2. A novel method for decoupling multi-axis F/M sensors is proposed based on ELM algorithm. The experiments illustrate that the ELM based decoupling method can attain higher accuracy while maintaining efficiency. Moreover, it is shown that the performance of the LS based decoupling method primarily depends on the application of a set of data that sufficiently spans the measurement range of the F/M sensor. This is not the case with the ELM and BPNN methods. Also, it was found that the proposed ELM based decoupling method requires less training time compared with BPNN.

## Acknowledgments

This work was supported in part by the National Nature Science Foundation of China(NSFC 61673163), Hunan provincial natural science foundation of China(2016JJ3045).

## References

[1] S. Mascaro, H.H. Asada, Measurement of finger posture and three-axis fingertip touch force using fingernail sensors, Rob. Autom. IEEE Trans. 20 (1) (2004) 26–35.
[2] A. Faragasso, A. Stilli, J. Bimbo, et al., Multi-axis stiffness sensing device for medical palpation, in: Intelligent Robots and Systems (IROS), 2015 IEEE/RSJ International Conference on, IEEE, 2015, pp. 2711–2716.
[3] Y.J. Han, Low-cost multi-touch sensing through frustrated total internal reflection, in: Proceedings of the 18th annual ACM symposium on User interface software and technology, ACM, 2005, pp. 115–118.
[4] Y. Noh, J. Bimbo, S. Sareh, et al., Multi-axis force/torque sensor based on simply–supported beam and optoelectronics, Sensors 16 (11) (2016) 1936.

[5] Q. Liang, D. Zhang, G. Coppola, et al., Multi-dimensional MEMS/micro sensor for force and moment sensing: a review, Sens. J. IEEE 14 (8) (2014) 2643–2657.
[6] L. Viry, A. Levi, M. Totaro, et al., Flexible three-axial force sensor for soft and highly sensitive artificial touch, Adv. Mater. 26 (17) (2014) 2659–2664.
[7] R.A. Brookhuis, H. Droogendijk, M.J. De Boer, et al., Six-axis force–torque sensor with a large range for biomechanical applications, J. Micromech. Microeng. 24 (3) (2014) 035015.
[8] C. Yuan, L.P. Luo, Q. Yuan, et al., Development and evaluation of a compact 6-axis force/moment sensor with a serial structure for the humanoid robot foot, Measurement 70 (2015) 110–122.
[9] M. Meng, Z. Wu, Y. Ge, et al., Design and characterization papers of a novel six-axis accelerometer, in: Intelligent Mechatronics and Automation, 2004. Proceedings. 2004 International Conference on, IEEE, 2004, pp. 574–578.
[10] M.K. Kang, S. Lee, J.H. Kim, Shape optimization of a mechanically decoupled six-axis force/torque sensor, Sens. Actuators A 209 (2014) 41–51.
[11] A.R. Tavakolpour-Saleh, M.R. Sadeghzadeh, Design and development of a three–component force/moment sensor for underwater hydrodynamic tests, Sens. Actuators A 216 (2014) 84–91.
[12] G. Lin, D. Wang, W. Zhang, et al., Research on the online initial value calibration method for the Wheel Force Transducer, IEEE Sens. J. 15 (2) (2015) 1043–1054.
[13] G. Palli, L. Moriello, U. Scarcia, et al., Development of an optoelectronic 6-axis force/torque sensor for robotic applications, Sens. Actuators A 220 (2014) 333–346.
[14] J. Lei, L. Qiu, M. Liu, et al., Application of neural network to nonlinear static decoupling of robot wrist force sensor, in: Intelligent Control and Automation, 2006. WCICA 2006. The Sixth World Congress on, 2, IEEE, 2006, pp. 5282–5285.
[15] X. Wen-bin, H. Cong, D. Wen-cai, Research on static characteristics of six-dimension force sensor, in: Computer Distributed Control and Intelligent Environmental Monitoring (CDCIEM), 2012 International Conference on, IEEE, 2012, pp. 577–581.
[16] B. Wu, P. Cai, Decoupling analysis of a sliding structure six-axis force/torque sensor, Meas. Sci. Rev. 13 (4) (2013) 187–193.
[17] T.A. Dwarakanath, B. Dasgupta, T.S. Mruthyunjaya, Design and development of a Stewart platform based force–torque sensor, Mechatronics 11 (7) (2001) 793–809.
[18] J. Ma, A. Song, J. Xiao, A robust static decoupling algorithm for 3-axis force sensors based on coupling error model and $\varepsilon$-SVR, Sensors 12 (11) (2012) 14537–14555.
[19] M. Turkseven, J. Ueda, Analysis of an MRI Compatible force sensor for sensitivity and precision, IEEE Sens. J. 13 (2) (Feb. 2013) 476–486.
[20] Q. Liang, D. Zhang, Y. Wang, et al., Development of a touch probe based on five-dimensional force/torque transducer for coordinate measuring machine (CMM), Rob. Comput. Integr. Manuf. 28 (2) (2012) 238–244.
[21] H.S. Efendioglu, T. Yildirim, K. Fidanboylu, Prediction of force measurements of a microbend sensor based on an artificial neural network, Sensors 9 (9) (2009) 7167–7176.
[22] G.B. Huang, Q.Y. Zhu, C.K. Siew, Extreme learning machine: theory and applications, Neurocomputing 70 (1) (2006) 489–501.